Low Temperature Processing of Iron Oxide Nanoflakes from Red Mud Extract toward Favorable De-arsenification of Water

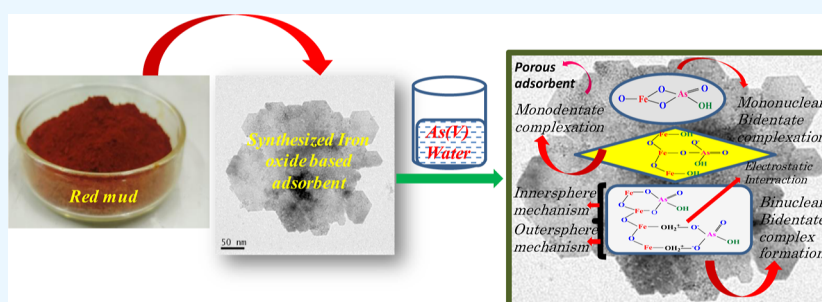Adwitiya Chakraborty, Prasanta Kumar Sinha, and Milan Kanti Naskar*

Read Online

ACCESS | Metrics & More | Article Recommendations | Supporting Information

ABSTRACT: Iron oxide (α-Fe$_2$O$_3$) was synthesized from red mud extract followed by hydrothermal reaction at 150 °C/6−24 h in the presence of NH$_4$OH. The crystallinity of α-Fe$_2$O$_3$ increased with reaction time as confirmed by X-ray Diffraction, while Fourier transform infrared spectroscopy and Raman illustrate the symmetric stretching vibration of the Fe−O bond in α-Fe$_2$O$_3$. The X-ray photoelectron spectroscopic analysis shows O 1s spectra at 530.6, 531.2, and 532 eV, signifying the lattice oxygen in Fe−O, surface oxygen defects, and oxygen in adsorbed hydroxyl groups, respectively. The morphology of α-Fe$_2$O$_3$ nanoflakes was noticed from field emission scanning electron microscopy and transmission electron microscopy. The developed particles reveal the BET surface area in the range of 136−347 m^2/g. The maximum As(V) adsorption capacity of 32−41 mg/g was obtained for adsorbent dose of 0.25 g/L. The arsenic level could be lowered down to 2−3 μg/L (<10 μg/L as per WHO's limit) with contaminated real water (64 μg/L) using 0.25 g/L of sample dose within 5 min of adsorption.

1. INTRODUCTION

Arsenic contamination in groundwater is a serious concern for the living beings. As a silent killer, arsenic (As) causes various complications in the human organ system like skin cancer, pigmentation, Blackfoot disease, cardiovascular disease, lungs, urinary bladder, kidney related ailments, and so forth.[1−3] The most common form of arsenic in natural water is oxyanions as arsenite (AsO$_3$$^{3−}$) and arsenate (AsO$_4$$^{3−}$) depending on redox conditions with pH, the former is more toxic than the latter.[4] However, the arsenate species [As(V)] mostly exists in surface water because of its thermodynamic stable form.[5] The World Health Organization (WHO) recommends the As concentration limit in drinking water to be 10 μg/L. Arsenic removal from ground water has been accomplished using a variety of techniques, including oxidation and sedimentation,[6] co-precipitation,[7] membrane separation,[8] coagulation and filtering,[9] ion exchange, reverse osmosis, electrolysis, adsorption, and many others.[10−14] Adsorption technology has shown promise for the removal of arsenic from water because of its simple design, ease of operation, high efficiency, greater regeneration ability, and wide applicability in small scale treatment plants.[15] Chutia et al. showed the adsorption capacity of zeolites of type H-MFI-24 (H24) and H-MFI-90 (H90) as 35.8 and 34.8 mg g$^{−1}$ for the removal of arsenic

starting with arsenic concentration of 10 mg/L at pH 6.5 using the sample dose of 2 g/L.[16] The maximum adsorption capacity of the MOF-based adsorbent material used in numerous studies on the adsorption of arsenic was found to be 90.92 mg g$^{−1}$, which could be attributed to the mesoporous structure facilitating mass transfer within the pores during the adsorption process.[17] Yao et al. showed the adsorption capacity of the iron oxide/activated carbon magnetic composite as 17.86 mg g$^{−1}$ with the initial As concentration of 10 mg/L at pH 6 for 60 min contact time using the sample dose of 5 g/L.[18] Arsenic and other hazardous ions were also shown to be very effectively removed by a polymer-based composite.[19] Layered double hydroxides,[20−22] hierarchical porous ZIF-8,[23] and iron-based materials[24−26] are found to be commonly used for As(V). Pintor et al. showed adsorption capacity of iron-coated cork granulates as 4.3 and 4.9 mg g$^{−1}$ for the removal of As(V) and As(III), respectively, with their initial concentration of 25
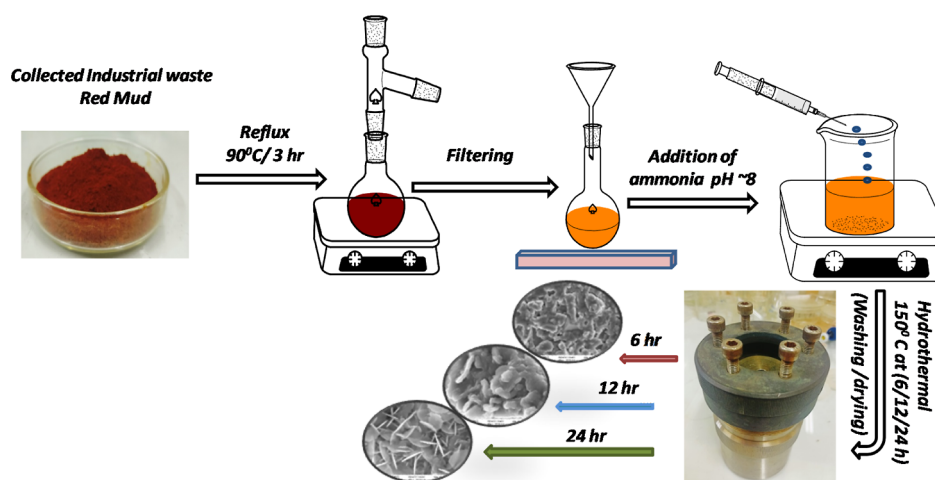
Figure 1. Schematic diagram for the preparation of iron oxide extracted from red mud.

mg/L at 20 °C for 24 h contact time using 2.5 g/L of sample dose.[24] Iron-based layered double hydroxides exhibited efficient arsenic adsorption due to their synergistic effect of the interlayered structure and the presence of iron containing metal−oxygen bonds, facilitating electrostatic interactions with arsenite/arsenate oxyanions.[27−30]

Arsenic removal from contaminated water using low cost adsorbents is highly demanding particularly in rural area community having low income. Babazad et al. used carbonized rice husk for the removal of lead and arsenic from aqueous solution.[31] Nguyen et al. reported arsenic removal from ground water using laterite.[32] Red mud is a waste product in aluminum industry. Red mud contains mainly iron and aluminum oxide/ hydroxides with a small amount of silica, TiO_2, Na_2O, and CaO.[33,34] The oxides/hydroxides of iron, aluminum, and titanium are effective for the adsorption of As(V). It is worth noting that raw red mud has lower arsenic adsorption capacity compared to modified red mud or synthesized iron oxides/ hydroxides as adsorbents. Numerous researchers have reported using modified red mud to successfully remove arsenic from an aqueous solution.[35−40] Recently, Xu et al. reported arsenic removal from aqueous solution using porous red mud beads.[41]

In the present work, we have extracted iron constituent from red mud by acid leaching followed by hydrothermal reaction in the presence of aqueous ammonia. Synthesis of iron oxide with a high surface area from red mud by a simple hydrothermal process without further heat treatment is rarely reported to the best of our knowledge. In this study, we have demonstrated that how the reaction time affects the crystallinity and surface properties of the material toward the adsorption efficiency of arsenic. The synthesized product was used for the removal of As(V) from aqueous solution. Kinetic studies were performed for the adsorption of arsenic by changing different parameters like concentration of adsorbates and adsorbents, time, pH, and temperature.

2. EXPERIMENTAL SECTION

2.1. Materials. The industrial waste red mud was collected from Utkal Aluminium International Ltd., Odisha, India. Hydrochloric acid (37%), ammonia (25%), and standard arsenic acid (H_3AsO_4, 1000 mg/L) were purchased from Merck, India, whereas sodium arsenate heptahydrate

($Na_2HAsO_4·7H_2O$, 98−102.0%) was collected from Loba Chemie Pvt. Ltd.

2.2. Preparation of Iron Oxide from Red Mud. Figure 1 shows schematic diagram for the preparation of iron oxide extracted from red mud. For the extraction of Fe(III) from red mud, 40 g of crushed red mud powder was leached with 400 mL of 6 M HCl under the reflux condition at 90 °C for 3 h. The leachate was separated out by centrifugation, and the concentration of Fe(III) was found to be 1 M. For the preparation of the iron oxide-based adsorbent, 10 mL of red mud extract was taken in a beaker followed by the dropwise addition of NH_4OH under stirring to raise the pH 8−9. A brown solid mass was obtained, which was diluted to 70 mL by adding Millipore water under the stirring condition. After 30 min of stirring, the whole dispersion was transferred into a Teflon-lined hydrothermal autoclave and was kept at 150 °C for 6−24 h. The brown colored products were collected by centrifugation and repeatedly washed with Millipore water followed by drying at 60 °C for 6 h. The samples are designated as FENH6, FENH12, and FENH24 for hydro-thermal treatment of 6, 12, and 24 h, respectively, at 150 °C.

2.3. Characterization. The synthesized materials were characterized by Fourier transform infrared (FTIR) spectros-copy (Spectrum two, PerkinElmer), Raman spectroscopy (Horiba T6400 spectrometer with 532 nm laser), X-ray diffraction (XRD) (Philips X'Pert Pro PW 3050/60, using Ni-filtered Cu Kα radiation, λ = 0.15418 nm), X-ray photo-electron spectroscopy (XPS) (PHI 5000 Versa Probe II, ULVAC-PHI with Al Kα radiation), X-ray fluorescence (XRF) (PANalytical, Axios, Almelo, Netherland), FESEM (Model: Zeiss, Supra 35VP, Oberkochen, Germany), and N_2 adsorption−desorption study Quantachrome (ASIQ MP), where the specific surface area was measured by the BET (Brunauer−Emmett−Teller) method, and pore size distribu-tions were calculated using the BJH (Barrett−Joyner−Halenda) method. The microstructural analysis of the samples was performed by field emission scanning electron microscopy (Model: Zeiss, Supra 35VP, Oberkochen, Germany) and transmission electron microscopy (TEM) (Tecnai G2 30ST (FEI).

2.4. Arsenic Adsorption Experiment. The adsorption kinetics study of arsenic from aqueous solution was performed
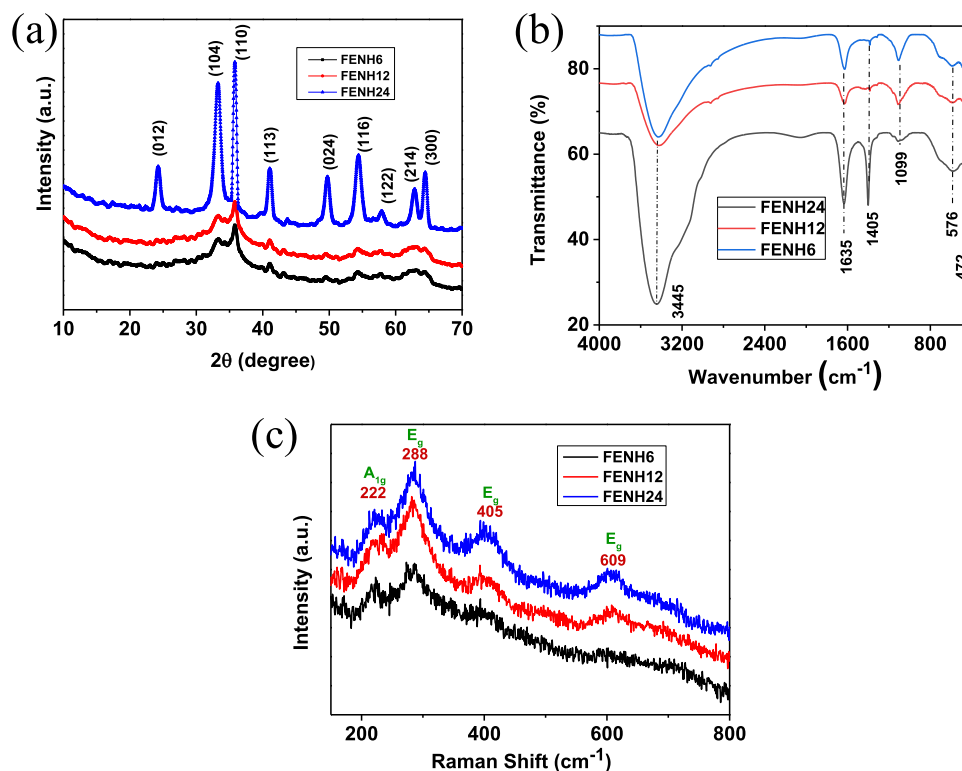
Figure 2. (a) XRD pattern, (b) FTIR, and (c) Raman spectra of α-Fe$_2$O$_3$.

by varying different parameters like contact time, initial arsenic concentration, sample dose, temperature, pH, and competing ions effect. The sample dose (adsorbent) was varied from 0.1 to 1 g/L with the initial arsenic concentration of 5 mg/L. For variation of time (5−180 min), pH (1.5−11.5) and temperature (303−343 K) effect, the sample dose was fixed at 0.25 g/L with the initial arsenic concentration of 2 mg/L and for competing ions (chloride, nitrate, sulfate, and phosphate), the initial concentration of each component was fixed around 5 mg/L with the sample dose of 1 gm/L. For the adsorption isotherm study, the initial As(V) concentration was varied from 2 to 20 mg/L with the sample dose of 0.50 g/L at equilibrium time of 180 min, temperature (303 K), and pH (6.5). The As(V) concentration after adsorption was determined by inductively coupled plasma atomic emission spectrometry (ICP−AES), ARCOS 130 MV, Spectro Analytical Instruments GmbH, Kleve, Germany and ICP mass spectrometry (ICP−MS), NexION 300X, PerkinElmer, USA.

The equilibrium adsorption capacity, q_e (mg/g), was determined from the following equation

$$q_e = (C_0 - C_e)(V/m) \tag{1}$$

where C_0 and C_e are the initial and final concentration of arsenic (mg/L), respectively, while V and m represent the solution volume in liter and mass in gram of the sample, respectively.

Noh and Schwarz's method[42] was adopted for determination of point of zero charge (pH$_{pzc}$). In this method, different sample quantities (5 mg to 2 g) were added each to 10 mL of 1 mM NaCl under stirring for 24 h followed by their pH measurement. A plot of pH vs sample mass was drawn in which pH approached to an asymptotic value by which the pH$_{pzc}$ of the sample was determined.

For the regeneration of the adsorbent, the exhausted adsorbent material was digested with 0.1 M NaOH for 24 h followed by repeated washing with Millipore water and drying. Thereafter for the recyclability test, 1 g/L of regenerated sample dose was stirred with 2 mg/L arsenic containing aqueous solution (20 mL) for 120 min at pH 6.5, which was performed with a total of five adsorption−desorption cycles.

3. RESULTS AND DISCUSSION

3.1. Study of the Crystal Structure. Figure 2a shows the XRD patterns of the sample obtained from hydrothermal treatment of red mud extract at 150 °C for 6−24 h. It confirms the crystalline phase of α-Fe$_2$O$_3$ with 2θ values of 24.27, 33.22, 35.77, 41.09, 49.74, 54.36, 57.91, 62.82, and 64.49 corresponding to hkl values of (012), (104), (110), (113), (024), (116), (018), (214), and (300), respectively (JCPDS file no. 86-0550). It is noticed that with the increasing reaction time, crystallinity of the α-Fe$_2$O$_3$ phase becomes higher. To ascertain the presence of other impurities in the prepared sample, XRF analysis was conducted. Table S1 shows that iron oxide and alumina contents were 81.4 and 14.29%, respectively, in the presence of a trace amount of other impurities. The FTIR study of the prepared samples obtained at 150 °C for 6−24 h is shown in Figure 2b. The appearance of vibration bands at 472 and 576 cm^{-1} is the signature of stretching vibration of the Fe−O bond.[43,44] A broad band at 1099 cm^{-1} indicates the stretching vibration of Fe−OH−Fe.[45] The absorption peaks at 1405 and 1635 cm^{-1} are ascribed to O−H bending vibration, while the absorption band at 3445 cm^{-1} is due to O−H stretching vibration of absorbed water molecules in the sample. However, in the instance of the sample FENH24, a shoulder peak is noticed at 3144 cm^{-1}.[46] This peak indicates that the hydrogen-bonded OH is in its stretching vibrational state. It is interesting to note that as
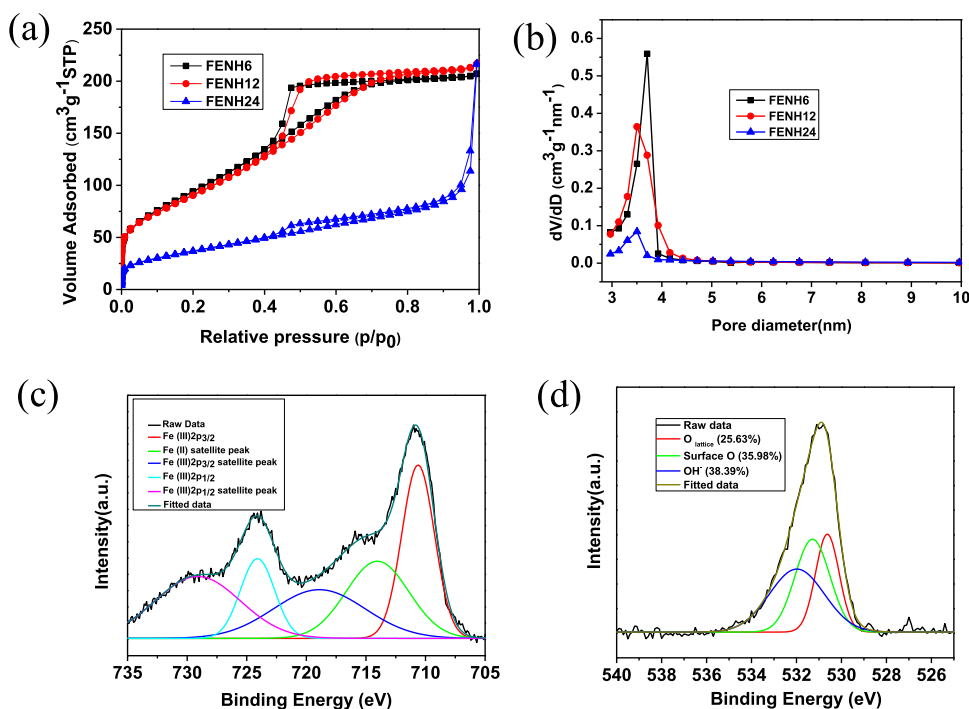
Figure 3. (a) BET isotherm, (b) BJH pore size distribution, and XPS spectra of α-Fe$_2$O$_3$: (c) Fe 2p and (d) O 1s of FENH24.

reaction time increases, polymeric association takes place, and hydrogen bonding plays a significant part in this process, which facilitates in the formation of the nanoflake structure.[47] Figure 2c shows Raman spectra of the products obtained at 150 °C for 6−24 h. The appearance of vibration band at 222 cm^{-1} corresponds to symmetric stretching vibration of Fe−O in A$_{1g}$ phonon mode. The bands at 288, 405, and 609 cm^{-1} are assigned to E$_g$ phonon mode of vibration, which are the signature of α-Fe$_2$O$_3$. It is reported that that hematite (α-Fe$_2$O$_3$) belonging to the $R3c$ space group generally exhibits seven phonon lines comprising two A$_{1g}$ and five E$_g$ phonon modes.[48,49] However, in the present study, we obtained four phonon mode of vibrations, i.e., one A$_{1g}$ and three E$_g$.

Figure 3a shows the BET isotherm of the hydrothermally treated sample at 150 °C for 6, 12, and 24 h reaction time. It is noticed that surface area values are maximum of 347 and 331 m^2/g for 6 and 12 h treated samples, respectively, followed by sudden decrease to 136 m^2/g for the 24 h treated sample. The BET curve shows a drastic decrease in the surface area for the sample FENH24, which could be understood by high crystallite growth and crystallinity at 24 h reaction time. For 6−12 h reaction time, crystallization occurs slowly, reflecting lower intensity of α-Fe$_2$O$_3$ peaks in the XRD pattern. In kinetically controlled systems, amorphous to crystalline phase transitions are frequent.[50] These transitions involve an initial fast-growing amorphous phase and a slow crystallization, resulting in a gradual trend in increasing crystallite size, which was found to be 2.1, 4.2, and 16.4 nm for FeNH6, FENH12, and FENH24, respectively. Therefore, a rapid increase in crystallite size from 4.2 to 16.4 nm for FENH12 and FENH24, respectively, lead to reduced surface area of the latter. The BET isotherms show type IV as per IUPAC classification, which is the signature mesoporous characteristics. However, the nature of hysteresis loops of the isotherm in 6−12 h samples is H2 type, signifying ink-bottle like mesopores, while that of the 24 h treated sample is H3 type, indicating slit-like

pores.[51] Interestingly, the total pore volume of the three samples heat-treated at 6, 12, and 24 h are comparable at around 0.33−0.36 cm^3/g, whereas the average pore diameter calculated from the BJH desorption plot (Figure 3b) are found in the range of 3.5−3.7 nm. It is worth noting that surface properties particularly, the surface area has a significant role toward the adsorption of water contaminants from aqueous solution. To investigate the surface chemical analysis, the XPS study was performed. Figure 3c,d shows XPS spectra of Fe 2p and O 1s, respectively, for the 24 h treated sample (FENH24). The appearance of peaks at around 710.6 and 724 eV could be attributed to the spin orbit doublets of Fe 2p$_{3/2}$ and Fe 2p$_{1/2}$, respectively,[52] confirming the existence of the Fe(III) state. The corresponding shake-up satellite peaks for Fe 2p$_{3/2}$ and Fe 2p$_{1/2}$ were found to be 719 and 729 eV, respectively (Figure 3c). Surprisingly, a satellite peak at around 715 eV confirms the existence of Fe(II); however, no primary peak for Fe(II) 2p$_{3/2}$ was noticed. It is demonstrated that the crystal structure of Fe$_2$O$_3$ contains Fe(II) sites, which could be originated via electron hopping.[53,54] The deconvoluted peaks of O 1s spectra are shown at 530.6, 531.2, and 532 eV (Figure 3d), signifying the lattice oxygen in Fe−O, surface oxygen defects, and oxygen in adsorbed hydroxyl groups, respectively,[45,55] with their percentage abundance of 25.7, 36, and 38.3% for the FENH24 sample. Figure S1 shows XPS spectra of FENH6 (6 h treated sample): (a) Fe 2p and (b) O 1s and FENH12 (12 h treated sample): (c) Fe 2p and (d) O 1s. The lattice oxygen, surface oxygen defects, and oxygen in adsorbed hydroxyl groups for FENH6 are 46.77, 25.05, and 28.17%, respectively, whereas those for FENH12 samples are found to be 48.08, 32.45, and 34.9%, respectively. It is worth mentioning that surface oxygen defects and oxygen in adsorbed hydroxyl groups are in increasing trend as FENH6 < FENH12 < FENH24. It could affect their adsorption efficiency for As(V). However, the surface area values of the samples follow as: FENH6 > FENH12 > FENH24, which demonstrate a
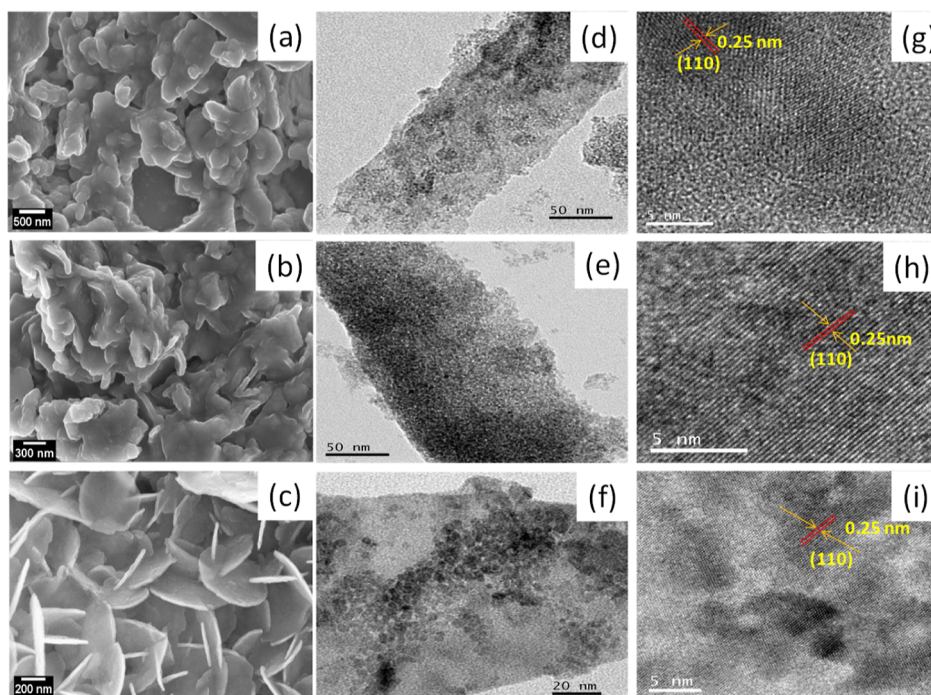
Figure 4. (a−c) FESEM images, (d−f) TEM images, and (g−i) HRTEM images of α-Fe$_2$O$_3$ particles.

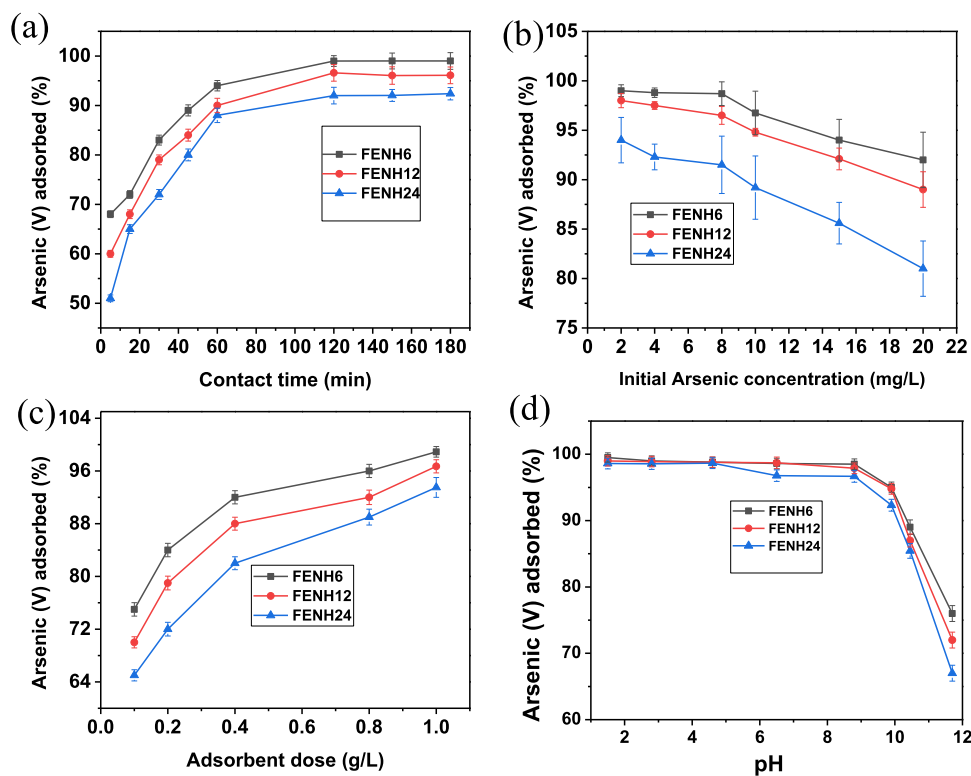**Figure 5.** Effect of (a) contact time, (b) initial As(V) concentration, (c) adsorbent dose, and (d) pH on the adsorption of As(V) ions by α-Fe$_2$O$_3$ particles.

pronounced effect on adsorption efficiency, superseding the effects of surface oxygen defects and oxygen in adsorbed hydroxyl groups.

Morphology of the synthesized products was examined by FESEM and TEM. Figure 4a−c shows the FESEM micro-structures obtained at 150 °C for different reaction times of 6, 12, and 24 h, respectively. It is noticed that for lower reaction

time (6 h), highly agglomerated particles are obtained. However, with the increase in reaction time of 12 h, nanoflake-like particles start growing. A complete nanoflake-like assembly with the petal-like structure of α-Fe$_2$O$_3$ was obtained for 24 h reaction time. During hydrothermal reaction at 150 °C, dissolution of the agglomerated particles takes place, rendering high entropy of the system. With the increasing
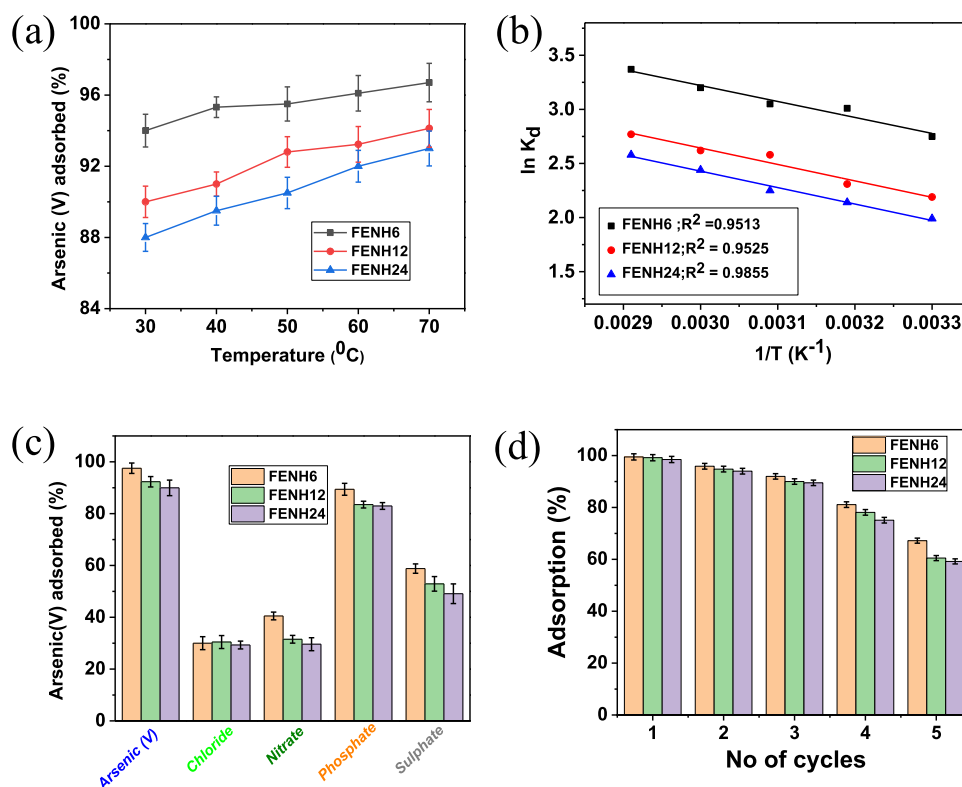
Figure 6. (a) Effect of temperature, (b) plot of ln K_d versus $1/T$, (c) co-existing ions effect, and (d) recyclability study for the adsorption for As(V) ions.

reaction time, the nascent nuclei start growing in a certain crystallographic orientation, generating a flake-like structure minimizing entropy of the system. The TEM image of the sample is shown in Figure 4d−f for 6, 12, and 24 h reaction time, respectively. It reveals the presence of nanopores in the samples. Interestingly, with a close observation of TEM microstructures, it is revealed that very tiny α-Fe$_2$O$_3$ particles of size in the range of 2−5 nm assembled in a petal-shaped particles, particularly for 24 h reaction time. The HRTEM images of α-Fe$_2$O$_3$ particles are shown in Figure 4g−i for three different reaction times of 6, 12, and 24 h, respectively. It indicates the lattice fringes of the (110) plane corresponding to the lattice spacing of 0.25 nm, which corroborated to the high intensity peak of α-Fe$_2$O$_3$ obtained from the XRD pattern (Figure 2a).

3.2. Arsenic Adsorption Study. *3.2.1. Effect of Contact Time.* The percentage adsorption of As(V) from aqueous solution with contact time is shown in Figure 5a, keeping the initial As(V) concentration of 2 mg/L (pH $\sim$ 6.8) with the sample dose of 0.25 g/L at 30 °C. It is noticed that the % adsorption of As(V) increased sharply up to 60 min of contact time, reaching equilibrium at 120 min of adsorption with % adsorption of 99, 96.6, and 92%, for the samples FENH6, FENH12, and FENH24 prepared at reaction times of 6, 12, and 24 h, respectively. Adsorption capacity (q_t) with time of the samples is shown in Figure S2a, which reaches maximum values of 7.9, 7.7, and 7.4 (mg/g) for FENH6, FENH12, and FENH24, respectively. It is demonstrated that the arsenic level could be lowered down to 2−3 μg/L (<10 μg/L as per WHO's limit) with contaminated real water (64 μg/L) using 0.25 g/L of sample dose within 5 min of adsorption. Figure S3 shows that the samples FENH6, FENH12, and FENH24 showed 96,

95, and 94.4% adsorption within a short time of adsorption (5 min), respectively.

3.2.2. Effect of the Initial As(V) Concentration. Figure 5b shows that the % adsorption is in decreasing trend with the increasing As(V) concentration from 2 to 20 mg/L (pH $\sim$ 6.8 at 30 °C for 120 min contact time) using 0.50 g/L of sample dosage. It is noteworthy that with the increasing As(V) concentration, the adsorption sites are getting shielded with the accumulation of contaminated ions, and co-ordination sites are becoming saturated, resulting in lower adsorption.[56,57] The adsorption capacity (q_e) is in increasing trend with the increasing initial arsenic concentrations (Figure S2b, Supporting Information).

3.2.3. Effect of Sample Dose. Figure 5c shows that with the increase in sample dose, the % adsorption is sharply increased up to 0.4 g/L of sample dosage followed by slow increase up to 1.0 g/L of adsorbent using 5 mg/L of As(V) contaminated water. With the increase in sample dose, there is abundance of adsorption sites, which facilitates more amount of As(V) adsorption uptake. However, the adsorption capacity (q_e) decreased with the increasing sample doses (Figure S2c, Supporting Information).

3.2.4. Effect of pH. The role of pH in aqueous solution is important for the adsorption of As(V) by the charged surface (positively charged H$^+$ ions and negatively charged OH$^-$ ions) of the adsorbent sample.[58] Figure 5d shows that using 2 mg/L arsenic contaminated water with the sample dose of 0.25 g/L, the adsorption (%) of As(V) remains almost constant (>96%) up to pH 8.8 for all the samples FENH6, FENH12, and FENH24, respectively. However, it falls sharply in alkaline pH (9.9−11.7) and reaches to minimum values of 76, 72, and 67% at pH 11.7 for the samples FENH6, FENH12, and FENH24, respectively. Interestingly, the adsorption capacity (q_e) of all

the samples remains practically the same of about 7.8 mg/g within a wide range of pH (1.5−8.8) followed by its sharp decrease within the pH range of 9.9−11.7 (Figure S2d, Supporting Information). To understand the effect of pH on As(V) adsorption, the measurement of point of zero charge (pH$_{PZC}$) of the sample is necessary. The pH$_{PZC}$ of the samples is found to be around 9.9 (Figure S4, Supporting Information). It is clear that below pH$_{PZC}$, there is abundance of the positively charged surface of the adsorbent, which helps facilitate to interact with the negatively charged species of As(V) through electrostatic attraction, rendering higher % adsorption and adsorption capacity. However, with increase in pH above pH$_{PZC}$ (pH > pH$_{PZC}$), the negatively charged surface repels the negatively charged adsorbate, decreasing the adsorption efficiency of the samples.

3.2.5. Effect of Temperature. For the temperature effect on As(V) adsorption, the initial As(V) concentration was kept at 2 mg/L with the sample dose of 0.25 g/L for 60 min of contact time at pH 6.8. Figure 6a shows that As(V) adsorption in aqueous solution increases with rise in temperature. Interestingly, the increasing trend was more significant for the sample FENH24 (synthesized for 24 h reaction time at 150 °C). Figure S2e (Supporting Information) also reveals that adsorption capacity increased with the rise in temperature. It is worth noting that the increase of As(V) adsorption efficiency with temperature signifies the endothermic process of adsorption, resulting in higher efficiency of As(V) adsorption.

3.2.6. Thermodynamic Investigation. The thermodynamic study on the As(V) adsorption process was carried out at different temperatures at 303, 313, 323, 333, and 343 K. The thermodynamic parameters like enthalpy (ΔH^0), entropy (ΔS^0), and Gibbs free energy (ΔG^0) were derived as follows

$$K_{eq}^0 = (C_0 - C_e)/C_e \tag{2}$$

$$\ln K_{eq}^0 = \Delta S^0/R - \Delta H^0/RT \tag{3}$$

$$\Delta G^0 = -RT \ln K_{eq}^0 \tag{4}$$

where K_{eq}^0 is the equilibrium constant, T (K) is the temperature, and R is the universal gas constant (8.314 J mol^{-1} K^{-1}).

By plotting $\ln K_{eq}^0$ vs $1/T$ from eq 3, the values of ΔH^0 and ΔS^0 can be obtained from the slope and intercept of the plot, respectively (Figure 6b). Table 1 shows the thermodynamic parameter values of ΔH^0, ΔS^0, and ΔG^0 for all the samples. The endothermic nature of the As(V) adsorption process was confirmed by positive values of ΔH^0. Furthermore, the positive values of ΔS^0 demonstrate that there prevails randomness at the solid−liquid interface during the adsorption process. The spontaneity of the adsorption process was confirmed by the negative values of ΔG^0. It is to be noted that with the increase in temperature, ΔG^0 values are becoming more and more negative, indicating favorable adsorption of As(V) with temperature,[59] and it is chemisorption rather than physisorption. It is to be noted that for the samples prepared at different temperatures, the values of ΔS^0 are comparable for the samples FENH12 and FENH24, while it is increased for the sample FENH6. However, $-\Delta G^0$ values are in the decreasing trend as FENH6 > FENH12 > FENH24. It indicates that with the increasing reaction time, the adsorption process by the sample is becoming less favorable due to lower ΔS^0 and $-\Delta G^0$ values, particularly for FENH24.

Table 1. Thermodynamic Parameters of Arsenic (V) Adsorption for Different Samples with Fixed Adsorbent Doses (0.25 g/L)

sample ID	ΔH^0 (kJ/mol)	ΔS^0 (J/mol K)	ΔG^0 (kJ/mol)
FENH6	+12.2698	+63.5189	−6.9947 at 303 K
			−7.6337 at 313 K
			−8.2727 at 323 K
			−8.9117 at 333 K
			−9.5577 at 343 K
FENH12	+12.6331	+59.8693	−5.265 at 303 K
			−5.855 at 313 K
			−6.445 at 323 K
			−7.035 at 333 K
			−7.625 at 343 K
FENH24	+12.6364	+58.0982	−4.9376 at 303 K
			−5.5176 at 313 K
			−6.0976 at 323 K
			−6.6776 at 333 K
			−7.2576 at 343 K

3.2.7. Effect of Co-existing Anions. In natural underground water, various co-existing ions may be present, which have susceptibility to compete with the arsenic at the active surface of the adsorbent. In this study, the effect of common co-existing ions such as chloride (Cl$^-$), nitrate (NO$_3^-$), phosphate (PO$_4^{3-}$), and sulfate (SO$_4^{2-}$) has been evaluated on the adsorption of As(V) using each contaminant concentration and sample dose of 5 mg/L and 1 g/L, respectively. Figure 6c shows that in the presence of the above co-existing anions, the % adsorptions for As(V) were 97.5, 92.3, and 89.9%, for the samples FENH6, FENH12, and FENH24, respectively, along with % removal of Cl$^-$, NO$_3^-$, PO$_4^{3-}$, and SO$_4^{2-}$ as 30−34, 47−50, 93−96, and 87−90%, respectively. It is noticed that the adsorption affinity for different anions with the adsorbent follows in the order of As(V) > PO$_4^{3-}$ > SO$_4^{2-}$ > NO$_3^-$ > Cl$^-$. Here, PO$_4^{3-}$ ions due to their same chemical nature with arsenate have a strong competitive effect with As(V) for adsorption sites of the adsorbent, inhibiting As(V) adsorption. The order of hydrated ionic radius of anions is SO$_4^{2-}$ > NO$_3^-$ > Cl$^-$. Therefore, SO$_4^{2-}$ ions due to their larger ionic radius form outer-sphere complexes with Fe(III) of the adsorbent through long-range electrostatic force compared to NO$_3^-$ and Cl$^-$ ions.

3.2.8. Recyclability Study. For minimizing the cost of water treatment and reusing the adsorbent materials after adsorption of As(V) contaminant water, the regeneration study is of utmost important. In this regard, the used adsorbent is treated with alkaline solution to exchange negatively charged arsenate (As(V)) with hydroxyl ions. Figure 6d shows the recyclability study of three different samples FENH6, FENH12, and FENH24. It illustrates that up to the third cycle, the adsorption is >90% followed by gradual fall of As(V) adsorption up to the fifth cycle, indicating the % adsorption of >60%. It is to be noted that after some cycles, the adsorption efficiency becomes lower because the adsorbed exchangeable hydroxide ions start trapping within the pore structure of the adsorbent, which are difficult to wash out with water. Therefore, adsorption is hindered due to electrostatic repulsion between negatively charged hydroxide and arsenate ions.

3.3. Adsorption Kinetics. For the kinetics study of adsorption, the experimental data were fitted with pseudo-first order and pseudo-second order models. The mathematical
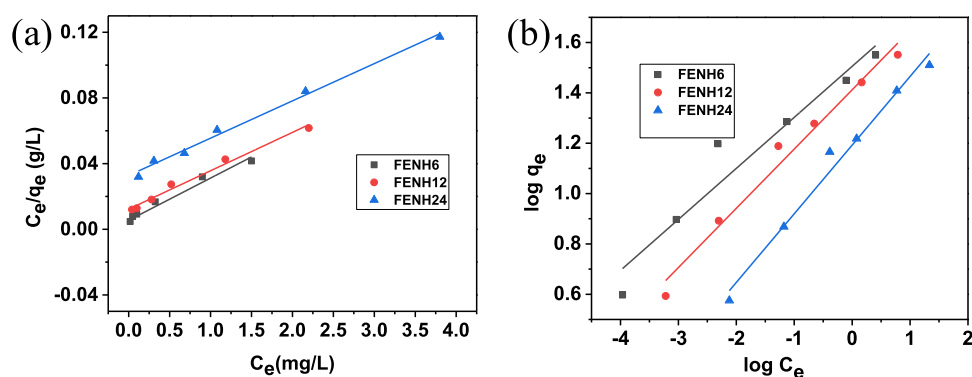
Figure 7. (a) Langmuir and (b) Freundlich isotherms for the adsorption for As(V) ions.

expression of the two models is shown in Table S2. From the pseudo-first order kinetics model, by plotting $\ln(q_e - q_t)$ vs t, the adsorption capacity at equilibrium (q_e) and rate constant (k_1) is evaluated from the intercept and slope, respectively. On the other hand, for pseudo-second order kinetics, the equilibrium adsorption capacity (q_e) and second order rate constant (k_2) are determined from the intercept and slope, respectively, by plotting t/q_t vs t. Figure S5a,b shows the linear fitting curves for pseudo-first-order and pseudo-second-order models, respectively. The relevant parameters obtained from pseudo-first order and pseudo-second order kinetics models are presented in Table S2. The correlation co-efficient (R^2) for the pseudo-second-order model approaches 1 with a high degree of linearity (best fitting curve), which signifies the chemisorption process for As(V) adsorption. The equilibrium adsorption capacity (q_e) was around 8 mg/g for three samples FENH6, FENH12, and FENH24 with a nominal decrease in values with the increase in reaction time for the preparation of adsorbent materials.

3.3.1. Adsorption Isotherms. To assess the adsorption performance of arsenic at the solid−liquid interface, Langmuir and Freundlich isotherm models were used. The linear expression of the two models is shown in Table S2. From Langmuir isotherm, by plotting C_e/q_e vs C_e, the maximum adsorption capacity $[q_m \text{ (mg/g)}]$ and Langmuir adsorption constant (K_L) are obtained from the slope and intercept, respectively (Figure 7a). By plotting $\log q_e$ vs $\log C_e$, in Freundlich isotherm, the adsorption intensity (n_F) and K_F (Freundlich constant) can be obtained from the slope and intercept, respectively (Figure 7b). The Langmuir isotherm illustrates that the adsorption process is uniform with monolayer formation, whereas Freundlich isotherm is considered for multilayer non-uniform and reversible adsorption. The relevant parameters determined from Langmuir and Freundlich isotherms are revealed in Table S3. The correlation coefficient R^2 (≥ 0.98) obtained from Langmuir isotherm indicates best fittings for As(V) adsorption as compared to Freundlich isotherm. It is noticed that the maximum adsorption capacity values calculated from Langmuir isotherm were found to be 41.1, 36.8, and 32 mg/g for the samples FENH6, FENH12, and FENH24, respectively, which were higher than those obtained from humic acid-grafted magnetic nanoparticles.[60] However, a study regarding the adsorption capacity compared to other adsorbent materials has also been done, which is represented in Table S4, exhibiting better adsorptivity of the synthesized α-Fe$_2$O$_3$.

3.4. Adsorption Mechanism. Surface property as well as ligand binding ability of the adsorbent materials play a pivotal role in the adsorption process. Iron oxide-based adsorbents are found to be prone to arsenic adsorption mainly due to their physico-chemical properties, which assists the adsorption of arsenic over a wide pH range. Figure 8 shows a proposed
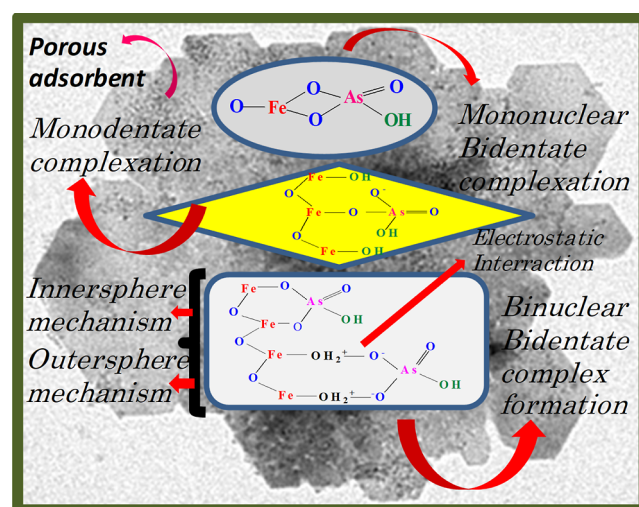

Figure 8. Proposed mechanism for the adsorption of As(V) ions by α-Fe$_2$O$_3$ particles.

mechanism for the adsorption of As(V) ions by α-Fe$_2$O$_3$ particles. It is demonstrated that arsenic adsorption on iron oxide-based materials occurs through the inner-sphere surface complex via monodentate, bidentate, or tridentate ligands and outer sphere surface complex. Inner sphere surface complexation takes place over a wide range of pH, i.e., below or above pH$_{PZC}$.[61] The outer sphere complexation is governed by electrostatic force of attraction between the negatively charged arsenate ions and positive surface of the iron oxide-based adsorbent. It is dominated at lower pH < pH$_{PZC}$. The Fe(III) in the Fe$_2$O$_3$ molecule can act as a Lewis acid because of the vacant d orbital, while arsenate ions with filled p electrons of oxygen behave as Lewis base. As a result, a dπ−pπ bonding occurs between the adsorbent molecules of iron oxide and binding ligands of arsenate during the formation of inner sphere complexes. However, the arsenate ions could bind to the adsorbent surface by the hydration layer with water molecules forming outer sphere complexes, where electrostatic interaction, van der Waals forces of attraction, hydrogen bonding, and so forth could led to a significant role for effective adsorption.[62] It is mentioned that as per XRF results, the alumina content in the synthesized product is less in

quantity (14.29%) as compared to Fe_2O_3 (81.4%). It is reported that in the presence of both iron oxide and aluminum oxide as adsorbents, iron oxide preferably adsorbed As(V).[63,64] During As(V) adsorption, iron oxide forms both the inner sphere and outer sphere complexation with arsenate species $(HAsO_4^{2-})$, while alumina as positively charged aluminum hydroxide species $[Al(OH)_3\text{-}2H]^{2+}$ interacts with arsenate species via electrostatic interaction (outer sphere complexation) only.[65] In the present work, iron oxide with its high concentration plays a more significant role for adsorption of As(V), which could supersede the adsorption ability of alumina. In order to comprehend the adsorption mechanism, Figure S6 depicts the FTIR study of the sample (FENH6) dose before and after As(V) adsorption. The emergence of a new peak at 858 cm^{-1} indicates the formation of As−O bonds during adsorption onto the Fe surface.[66]

4. CONCLUSIONS

We have prepared iron oxide nanoflakes from red mud extract by hydrothermal reaction at low temperature (150 °C/6−24 h). The synthesized product was utilized for the adsorption of As(V) from aqueous solution. For competitive ions effect, the adsorption affinity for different anions with the adsorbent follows in the order of As(V) > PO_4^{3-} > SO_4^{2-} > NO_3^- > Cl^-. The spontaneity of the adsorption process was confirmed by the negative values of ΔG^0, favoring adsorption of As(V) via a chemisorption process. The pseudo-second order kinetics and Langmuir isotherm models exhibit the best fitting for the adsorption of As(V). Arsenic adsorption on iron oxide-based materials occurs through the inner-sphere surface complex via monodentate, bidentate, or tridentate ligand and outer sphere surface complex by electrostatic interaction, van der Waals force of attraction, hydrogen bonding, and so forth. The present study shows a direction for fabrication of iron oxide-based nanoadsorbents using industrial wastes for effective performance of de-arsenification of water.

■ ASSOCIATED CONTENT

ⓢ Supporting Information

The Supporting Information is available free of charge at https://pubs.acs.org/doi/10.1021/acsomega.3c02689.

> XPS spectra of (a) Fe (2p), (b) O (1s) for the FENH6 sample and (c) Fe (2p), (d) O (1s) for the FENH12 sample; adsorption capacity with (a) contact time, (b) initial arsenic (v) concentration, (c) adsorbent dose, (d) pH, and (e) temperature on the adsorption of As(V) by α-Fe_2O_3; change of pH with % mass (W/V); kinetics data with linear fitting of (a) pseudo-first-order and (b) pseudo-second-order; FTIR spectra of the FENH6 sample before and after As(V) adsorption; XRF analysis of sample FENH24; kinetic parameters for the adsorption of As(V) for adsorbent dose of 0.25 g/L; parameters obtained from Langmuir and Freundlich models; and comparative data on maximum adsorption capacity for As (V) adsorption by the synthesized α-Fe_2O_3 and reported adsorbents (PDF)

■ AUTHOR INFORMATION

Corresponding Author

Milan Kanti Naskar − *Central Glass and Ceramic Research Institute (CSIR), Kolkata 700 032, India;* ⓘ orcid.org/0000-0002-7447-4941; Email: milan@cgcri.res.in

Authors

Adwitiya Chakraborty − *Central Glass and Ceramic Research Institute (CSIR), Kolkata 700 032, India*

Prasanta Kumar Sinha − *Central Glass and Ceramic Research Institute (CSIR), Kolkata 700 032, India*

Complete contact information is available at: https://pubs.acs.org/10.1021/acsomega.3c02689

Notes

The authors declare no competing financial interest.

■ REFERENCES

(1) Mohammed Abdul, K. S.; Jayasinghe, S. S.; Chandana, E. P. S.; Jayasumana, C.; De Silva, P. M. C. S. Arsenic and human health effects: a review. *Environ. Toxicol. Pharmacol.* **2015**, *40*, 828−846.

(2) Sarkar, A.; Paul, B. Corrigendum to "The global menace of arsenic and its conventional remediation − A critical review" [Chemosphere 158 (September) (2016) 37−49]. *Chemosphere* **2017**, *173*, 630−631.

(3) Sandoval, M. A.; Fuentes, R.; Nava, J. L.; Coreño, O.; Li, Y.; Hernández, J. H. Simultaneous removal of fluoride and arsenic from groundwater by electrocoagulation using a filter-press flow reactor with a three-cell stack. *Sep. Purif. Technol.* **2019**, *208*, 208−216.

(4) Liu, J.; Wu, P.; Li, S.; Chen, M.; Cai, W.; Zou, D.; Zhu, N.; Dang, Z. Synergistic deep removal of As(III) and Cd(II) by a calcined multifunctional MgZnFe-CO$_3$ layered double hydroxide: Photo-oxidation, precipitation and adsorption. *Chemosphere* **2019**, *225*, 115−125.

(5) Akin, I.; Arslan, G.; Tor, A.; Ersoz, M.; Cengeloglu, Y. Arsenic(V) removal from underground water by magnetic nano-particles synthesized from waste red mud. *J. Hazard. Mater.* **2012**, *235−236*, 62−68.

(6) Bisceglia, K. J.; Rader, K. J.; Carbonaro, R. F.; Farley, K. J.; Mahony, J. D.; Di Toro, D. M. Iron (II)-catalyzed oxidation of arsenic(III) in a sediment column. *Environ. Sci. Technol.* **2005**, *39*, 9217−9222.

(7) De Klerk, R. J.; Jia, Y.; Daenzer, R.; Gomez, M. A.; Demopoulos, G. P. Continuous circuit coprecipitation of arsenic (V) with ferric iron by lime neutralization: Process parameter effects on arsenic removal and precipitate quality. *Hydrometallurgy* **2012**, *111−112*, 65−72.

(8) Uddin, M. T.; Mozumder, M. S. I.; Figoli, A.; Islam, M. A.; Drioli, E. Arsenic removal by conventional and membrane technology: An overview. *Indian J. Chem. Technol.* **2007**, *14*, 441−450.

(9) Kumar, I.; Quaff, A. R. Comparative study on the effectiveness of natural coagulant aids and commercial coagulant: removal of arsenic from water. *Int. J. Environ. Sci. Technol.* **2019**, *16*, 5989−5994.

(10) Cheng, Z.; Fu, F.; Dionysiou, D. D.; Tang, B. Adsorption,oxidation, and reduction behavior of arsenic in the removal of aqueous As (III) by mesoporous Fe/Al bimetallic particles. *Water Res.* **2016**, *96*, 22−31.

(11) Misra, R. K.; Jain, S. K.; Khatri, P. K. Iminodiacetic acidfunctionalized cation exchange resin for adsorptive removal of Cr(VI), Cd (II), Ni (II) and Pb (II) from their aqueous solutions. *J. Hazard. Mater.* **2011**, *185*, 1508−1512.

(12) Abejón, A.; Garea, A.; Irabien, A. Arsenic removal from drinking water by reverse osmosis: Minimization of costs and energy consumption. *Sep. Purif. Technol.* **2015**, *144*, 46−53.

(13) Yuan, S.; Xie, S.; Zhao, K.; Gan, Y.; Wang, Y. Field tests of in-well electrolysis removal of arsenic from high phosphate and iron groundwater. *Sci. Total Environ.* **2018**, *644*, 1630−1640.

(14) He, S.; Han, C.; Wang, H.; Zhu, W.; He, S.; He, D.; Luo, Y. Uptake of Arsenic(V) Using Alumina Functionalized Highly Ordered Mesoporous SBA-15 (Al_x-SBA-15) as an Effective Adsorbent. *J. Chem. Eng. Data* **2015**, *60*, 1300−1310.

(15) Niazi, N. K.; Bibi, I.; Shahid, M.; Ok, Y. S.; Shaheen, S. M.; Rinklebe, J.; Wang, H.; Murtaza, B.; Islam, E.; Farrakh Nawaz, M.; Lüttge, A. Arsenic removal by Japanese oak wood biochar in aqueous solutions and well water: investigating arsenic fate using integrated spectroscopic and microscopic techniques. *Sci. Total Environ.* **2018**, *621*, 1642−1651.

(16) Chutia, P.; Kato, S.; Kojima, T.; Satokawa, S. Arsenic adsorption from aqueous solution on synthetic zeolites. *J. Hazard. Mater.* **2009**, *162*, 440−447.

(17) Li, J.; Hayat, T.; Zhao, G.; Chen, C.; Chai, Z.; Alsaedi, A.; Wang, X.; Wang, X. Metal−organic framework-based materials: superior adsorbents for the capture of toxic and radioactive metal ions. *Chem. Soc. Rev.* **2018**, *47*, 2322−2356.

(18) Yao, S.; Liu, Z.; Shi, Z. Arsenic removal from aqueous solutions by adsorption onto iron oxide/activated carbon magnetic composite. *J. Environ. Health Sci. Eng.* **2014**, *12*, 58.

(19) Zhao, G.; Huang, X.; Tang, Z.; Huang, Q.; Niu, F.; Wang, X. K. Polymer-based nanocomposites for heavy metal ions removal from aqueous solution: a review. *Polym. Chem.* **2018**, *9*, 3562−3582.

(20) Kundu, S.; Chowdhury, I. H.; Naskar, M. K. Hierarchical Porous Carbon Nanospheres for Efficient Removal of Toxic Organic Water Contaminants of Phenol and Methylene Blue. *J. Chem. Eng. Data* **2018**, *63*, 559−573.

(21) Huang, Y.; Liu, Z. .; Bo, A. .; Tang, X.; Martens, W.; Kou, L.; Gu, Y.; Carja, G.; Zhu, H.; Sarina, S. High efficient arsenic removal by In-layer sulphur of layered double hydroxide. *Colloid Interface Sci.* **2022**, *608*, 2358−2366.

(22) Hongtao, L.; Shuxia, L.; Hua, Z.; Yanling, Q.; Daqiang, Y.; Jianfu, Z.; Zhiliang, Z. Comparative study on synchronous adsorption of arsenate and fluoride in aqueous solution onto MgAlFe-LDHs with different intercalating anions. *RSC Adv.* **2018**, *8*, 33301−33313.

(23) Shi, L.; Shu, Z.; Wang, K.; Zhou, J.; Li, T. Nanoporous Zeolitic Imidazolate Framework-8 nanoparticles for arsenic removal. *ACS Appl. Nano Mater.* **2023**, *6*, 1744−1754.

(24) Pintor, A. M. A.; Vieira, B. R. C.; Santos, S. C. R.; Boaventura, R. A. R.; Botelho, C. M. Arsenate and arsenite adsorption onto iron-coated cork granulates. *J. Environ. Chem. Eng.* **2018**, *642*, 1075−1089.

(25) Li, F.; Guo, H.; Zhou, X.; Zhao, K.; Shen, J.; Liu, F.; Wei, C. Impact of natural organic matter on arsenic removal by modified granular natural siderite: Evidence of ternary complex formation by HPSEC-UV-ICP-MS. *Chemosphere* **2017**, *168*, 777−785.

(26) Wang, Y.; Zhang, P.; Zhang, T. C.; Xiang, G.; Wang, X.; Pehkonen, S.; Yuan, S. A magnetic γ-Fe_2O_3@PANI@TiO_2 core−shell nanocomposite for arsenic removal *via* a coupled visible-light-induced photocatalytic oxidation−adsorption process. *Nanoscale Adv.* **2020**, *2*, 2018−2024.

(27) Yu, L.; Liu, H.; Liu, C.; Lan, H.; Qu, J. Magnetically-Confined Fe-Mn Bimetallic Oxide Encapsulation as an Efficient and Recoverable Adsorbent for Arsenic(III) Removal. *Part. Part. Syst. Charact.* **2016**, *33*, 323−331.

(28) Zhang, G.; Xu, X.; Ji, Q.; Liu, R.; Liu, H.; Qu, J.; Li, J. Porous Nanobimetallic Fe−Mn Cubes with High Valent Mn and Highly Efficient Removal of Arsenic(III). *ACS Appl. Mater. Interfaces* **2017**, *9*, 14868−14877.

(29) Lu, H.; Zhu, Z.; Zhang, H.; Zhu, J.; Qiu, Y. Simultaneous removal of arsenate and antimonate in simulated and practical water samples by adsorption onto Zn/Fe layered double hydroxide. *Chem. Eng. J.* **2015**, *276*, 365−375.

(30) Irawan, C.; Sari, A. R.; Yulianingtias, A.; Melinda, R. A.; Mirwan, A. Application of Mn-Fe Layered Double Hydroxide as an Adsorbent for the Removal of Arsenic from Synthetic Acid Mine Drainage. *J. Rekayasa Kimia Lingkungan* **2021**, *16*, 45−51.

(31) Babazad, Z.; Kaveh, F.; Ebadi, M.; Mehrabian, R. Z.; Juibari, M. H. Efficient removal of lead and arsenic using macromolecule-carbonized rice husks. *Heliyon* **2021**, *7*, No. e06631.

(32) Nguyen, T. H.; Tran, H. N.; Vu, H. A.; Trinh, M. V.; Nguyen, T. V.; Loganathan, P.; Vigneswaran, S.; Nguyen, T. M.; Trinh, V. T.; Vu, D. L.; Nguyen, T. H. H. Laterite as a low-cost adsorbent in a sustainable decentralized filtration system to remove arsenic from groundwater in Vietnam. *Sci. Total Environ.* **2020**, *699*, 134267.

(33) Sanchez-Segado, S.; Mankanyire, T.; Esucufero-Castejon, L.; Hara, Y.; Jha, A. Reclamation of reactive metal oxides from complex minerals using alkali roasting and leaching-an improved approach to process engineering. *Green Chem.* **2015**, *17*, 2059−2080.

(34) Khairul, M. A.; Zanganeh, J.; Moghtaderi, B. The composition, recycling and utilisation of Bayer red mud. *Resour., Conserv. Recycl.* **2019**, *141*, 483−498.

(35) Roy, J. S.; Bhattacharya, G.; Chauhan, D.; Deshmukh, S.; Upadhyay, R.; Priyadarshini, R.; Sinha Roy, S. Potential use of smartly engineered red mud nanoparticles for removal of arsenate and pathogens from drinking water. *SN Appl. Sci.* **2020**, *2*, 796.

(36) Joseph, C. G.; Taufiq-Yap, Y. H.; Krishnan, V.; Puma, G. L. Application of modified red mud in environmentally-benign applications: A review paper. *Environ. Eng. Res.* **2020**, *25*, 795−806.

(37) Wu, C.; Huang, L.; Xue, S. G.; Huang, Y. Y.; Hartley, W.; Cui, M.; Wong, M. H. Arsenic sorption by red mud-modified biochar produced from rice straw. *Environ. Sci. Pollut. Res. Int.* **2017**, *24*, 18168−18178.

(38) Biswas, R.; Sarkar, A. A two-step approach for arsenic removal by exploiting an autochthonous Delftia sp. BAs29 and neutralized red mud. *Environ. Sci. Pollut. Res.* **2021**, *28*, 40665−40677.

(39) Yang, D.; Sasaki, A.; Endo, M. Solidification/Stabilization of Arsenic in Red Mud upon Addition of Fe (III) or Fe (III) and Al (III) Dissolved in H_2SO_4. *J. Water Environ. Technol.* **2018**, *16*, 115−126.

(40) Shoppert, A. A.; Loginova, I. V.; Rogozhnikov, D. A.; Karimov, K. A.; Chaikin, L. I. Increased As Adsorption on Maghemite-Containing Red Mud Prepared by the Alkali Fusion-Leaching Method. *Minerals* **2019**, *9*, 60.

(41) Xu, Y.; Yin, Y.; Guo, M.; Xu, G.; Li, L.; Liu, C. Enhanced removal of arsenic from aqueous solution by novel red mud porous beads: batch and column experiments. *Water Supply* **2022**, *22*, 3980−3992.

(42) Noh, J. S.; Schwarz, J. A. Estimation of the Point of Zero Charge of Simple Oxides by Mass Titration. *J. Colloid Interface Sci.* **1989**, *130*, 157−164.

(43) Raja, K.; Mary Jaculine, M.; Jose, M.; Verma, S.; Prince, A. A. M.; Ilangovan, K.; Sethusankar, K.; Jerome Das, S. Sol−gel synthesis and characterization of α-Fe2O3 nanoparticles. *Superlattices Microstruct.* **2015**, *86*, 306−312.

(44) Roy, M.; Naskar, M. K. Alkali metal ion induced cube shaped mesoporous hematite particles for improved magnetic properties and efficient degradation of water pollutants. *Phys. Chem. Chem. Phys.* **2016**, *18*, 20528−20541.

(45) Gao, J.-M.; Wang, B.; Li, W.; Cui, L.; Guo, Y.; Cheng, F. High-efficiency leaching of Al and Fe from fly ash for preparation of polymeric aluminum ferric chloride sulfate coagulant for wastewater treatment. *Sep. Purif. Technol.* **2023**, *306*, 122545.

(46) Loaiza-Gil, A.; Arenas, J.; Villarroel, M.; Imbert, F.; del Castillo, H.; Fontal, B. Heavier alcohols synthesis on cobalt phyllosilicate catalysts. *J. Mol. Catal. A: Chem.* **2005**, *228*, 339−344.

(47) Zhong, L.-S.; Hu, J.-S.; Cao, A.-M.; Liu, Q.; Song, W.-G.; Wan, L.-J. 3D Flowerlike Ceria Micro/Nanocomposite Structure and Its Application for Water Treatment and CO Removal. *Chem. Mater.* **2007**, *19*, 1648−1655.

(48) Reveendran, R.; Khadar, M. A. Structural optical and electrical properties of Cu doped α-Fe_2O_3 nanoparticles. *Mater. Chem. Phys.* **2018**, *219*, 142−154.

(49) Testa-Anta, M.; Ramos-Docampo, M. A.; Comesaña-Hermo, M.; Rivas-Murias, B.; Salgueirino, V. Raman spectroscopy to unravel the magnetic properties of iron oxide nanocrystals for biorelatedapplications. *Nanoscale Adv.* **2019**, *1*, 2086−2103.

(50) Carter, J. L.; Cusumano, J. A.; Sinfelt, J. H. Catalysis over Supported metalsV. the effect of Crystallite size on the catalytic activity of Nickel. *J. Phys. Chem.* **1966**, *70*, 2257−2263.

(51) Ghosh, S.; Das, R.; Naskar, M. K. Morphologically tuned aluminum hydrous oxides and their calcined products. *J. Am. Ceram. Soc.* **2016**, *99*, 2273−2282.

(52) Zhang, D.; Fan, X.; Yang, A.; Zong, X. Hierarchical assembly of urchin-like alpha-iron oxide hollow microspheres and molybdenum disulphide nanosheets for ethanol gas sensing. *J. Colloid Interface Sci.* **2018**, *523*, 217−225.

(53) Wu, X.; Zhang, Z. Z.; Liang, Q. S.; Meng, J. Evolution from(110)Feto(111)Fe3O4 thin filmsgrownbymagnetron sputtering usingFe2O3 target. *J. Cryst. Growth* **2012**, *340*, 74−77.

(54) Wu, K.; Lu, Y.; Liu, Y.; Liu, Y.; Shen, M.; Debliquy, M. Synthesis and acetone sensing properties of copper (Cu2+) substituted zinc ferrite hollow micro-nanospheres. *Ceram. Interfaces* **2020**, *46*, 28835−28843.

(55) Roy, M.; Basak, S.; Naskar, M. K. Bi-template assisted synthesis of mesoporous manganese oxide nanostructures: Tuning properties for efficient CO oxidation. *Phys. Chem. Chem. Phys.* **2016**, *18*, 5253−5263.

(56) Chakraborty, A.; Naskar, M. K. Sol−gel synthesis of alumina gel@zeolite X nanocomposites for high performance water defluoridation: batch and column adsorption study. *Mater. Adv.* **2022**, *3*, 8544−8556.

(57) Teimouri, A.; Ghanavati Nasab, S.; Habibollahi, S.; Fazel-Najafabadi, M.; Chermahini, A. N. Synthesis and characterization of a chitosan/montmorillonite/ZrO$_2$ nanocomposite and its application as an adsorbent for removal of fluoride. *RSC Adv.* **2015**, *5*, 6771−6781.

(58) Alchouron, J.; Navarathna, C.; Chludil, H. D.; Dewage, N. B.; Perez, F.; Hassan, E. B.; Pittman Jr, C. U.; Vega, A. S.; Mlsna, T. E. Assessing South American Guadua chacoensis bamboo biochar and Fe3O4 nanoparticle dispersed analogues for aqueous arsenic(V) remediation. *Sci. Total Environ.* **2020**, *706*, 135943.

(59) He, J.; Cai, X.; Chen, K.; Li, Y.; Zhang, K.; Jin, Z.; Meng, F.; Liu, N.; Wang, X.; Kong, L.; Huang, X.; Liu, J. Performance of a novelly-defined zirconium metal-organic frameworks adsorption membrane in fluoride removal. *Colloid Interface Sci.* **2016**, *484*, 162−172.

(60) Rashid, M.; Sterbinsky, G. E.; Pinilla, M. A. G.; Cai, Y.; O'Shea, K. E. Kinetic and Mechanistic Evaluation of Inorganic Arsenic Species Adsorption onto Humic Acid Grafted Magnetite Nanoparticles. *J. Phys. Chem. C* **2018**, *122*, 13540−13547.

(61) Aredes, S.; Klein, B.; Pawlik, M. The removal of arsenic from water using natural iron oxide minerals. *J. Cleaner Prod.* **2013**, *60*, 71−76.

(62) Hao, L.; Liu, M.; Wang, N.; Li, G. A critical review on arsenic removal from water using iron-based adsorbents. *RSC Adv.* **2018**, *8*, 39545−39560.

(63) Jeong, Y.; Maohong, F.; Leeuwen, J. V.; Belczyk, J. F. Effect of competing solutes on arsenic (V) adsorption using iron and aluminium oxides. *J. Environ. Sci.* **2007**, *19*, 910−919.

(64) Jeong, Y.; Fan, M.; Singh, S.; Chuang, C.-L.; Saha, B.; Hans van Leeuwen, J. Evaluation of iron oxide and aluminum oxide as potential arsenic(V) adsorbents. *Chem. Eng. Process.* **2007**, *46*, 1030−1039.

(65) Han, C.; Li, H.; Pu, H.; Yu, H.; Deng, L.; Huang, S.; Luo, Y. Synthesis and characterization of mesoporous alumina and their performances for removing arsenic(V). *Chem. Eng. J.* **2013**, *217*, 1−9.

(66) Zhou, Z.; Liu, Y. G.; Liu, S. B.; Liu, H. y.; Zeng, G. m.; Tan, X. f.; Yang, C. p.; Ding, Y.; Yan, Z. l.; Cai, X. x. Sorption performance and mechanisms of arsenic(V) removal by magnetic gelatin-modified biochar. *J. Chem. Eng.* **2017**, *314*, 223−231.